Nature of the spin liquid in underdoped cuprate superconductors

Y. A. Kharkov and O. P. Sushkov

School of Physics, University of New South Wales, Sydney 2052, Australia

In the present paper, we address a long-standing problem of the magnetic ground state and magnetic excitations in underdoped cuprates. Modeling cuprates by the extended $t - J$ model, we show that there is a dimensionless parameter λ which drives quantum magnetic criticality at low doping x. Hence we derive the zero temperature $\lambda - x$ phase diagram of the model. It is argued that all underdoped cuprates are close to the quantum tricritical point $x = 0$, $\lambda = 1$. The three phases "meet" at the tricritical point: (i) Néel antiferromagnet, (ii) spin spiral with antinodal direction of the spiral wave vector, (iii) algebraic spin liquid. We argue that underdoped cuprates belong either to the spin-liquid phase or they are on the borderline between the spin liquid and the spin spiral. We calculate the energy position E_{cross} of the inelastic neutron scattering response maximum at $q = (\pi, \pi)$ and compare our results with experiments. We also explain softening of magnons in the intermediate regime observed in inelastic neutron scattering.

I. INTRODUCTION

It is widely believed that an understanding of the nature of magnetic ground state and spin excitations in cuprates is crucial for resolving the problem of high Tc superconductivity. The most striking physics arises in hole-doped cuprates in the regime of low doping, where exotic phase transitions between distinct magnetic states take place. Intricate details of doping-driven transitions remain elusive and lack a unifying picture. There are two major cuprate families, $La_{2-x}Sr_xCuO_4$ (LSCO) and $YBa_2Cu_3O_{6+y}$ (YBCO) that are best experimentally studied in the low doping regime. For a review of experimental data on magnetic excitations in these compounds see Ref. [1] and also Refs. [2–4]. While there are numerous material specific details (dependent on the degree of disorder, number of CuO_2 planes, oxygen chains, etc.), the most prominent and generic phenomenological observations can be summarized as follows: (i) A commensurate antiferromagnetic (AFM) phase persist at very low doping. (ii) An intermediate state historically called the "spin glass" state arises in the doping window from a few percent to about 10%. The spin glass phase is characterized by very small static or quasistatic magnetic moments. (iii) At higher values of doping, the static magnetic moment vanishes. (iv) Magnetic response in the magnetically disordered phase is always incommensurate and manifests the famous "hourglass" dispersion. (v) The onset of superconductivity upon increasing of doping always occurs in the "spin glass" phase.

On the theoretical side, it is widely accepted that the most important low-energy physics of cuprates is described by the extended $t - J$ model [5–7]. Magnetic phase diagram of the $t - J$ model at the classical mean-field level, i.e., disregarding quantum fluctuations of spins, is well understood [8,9]. Besides doping x, another important parameter is $\lambda \propto g^2 m^*$, where g is the hole-magnon interaction constant and m^* is the hole's effective mass. In a lightly doped $t - J$ model, holes always form small pockets near four nodal points in the

Brillouin zone $\boldsymbol{k}_0 = (\pm \pi/2, \pm \pi/2)$ and $\boldsymbol{k}_0 = (\pm \pi/2, \mp \pi/2)$, and m^* describes curvature of the holon dispersion near the minima points. The explicit relation of λ to parameters of the extended $t - J$ model was derived in Ref. [10] and will be specified later. The zero temperature $\lambda - x$ mean-field phase diagram of the model is shown in Fig. 1(a).

The Lifshitz point at $\lambda_{\text{LP}} = 1$ (at which a transition between commensurate and incommensurate spin states occurs) separates two phases: (i) the Néel phase at $\lambda < 1$ and (ii) the static spin-spiral phase at $1 < \lambda < 2$. On the $x - \lambda$ phase diagram, the Lifshitz point becomes a Lifshitz line. The direction of the spin spiral is always antinodal, i.e., $\mathbf{Q} = (Q, 0)$ or $\mathbf{Q} = (0, Q)$, and the wave vector of the spiral scales linearly with doping, $Q \propto x$, Ref. [8]. When further increasing the coupling parameter λ, the system becomes unstable toward phase separation at $\lambda_{\text{PS}} = 2$, Ref. [9] A possibility of a noncoplanar state at $1 < \lambda < 2$ has been also considered [9]; however, the noncoplanar phase was ruled out in favour of the spin-spiral state, see Ref. [11].

In the mean field paradigm resulting in the phase diagram of the $t - J$ model in Fig. 1(a), quantum fluctuations of spins are completely ignored. On the other hand, in the vicinity of the Lifshitz point, quantum fluctuations are strongly enhanced and can lead to quantum phase transitions. Some 30 years ago, Ioffe and Larkin considered a seemingly unrelated problem [12] of a Lifshitz transition in a two-dimensional (2D) frustrated antiferromagnet (nonitinerant) between the collinear AFM phase and the spin-spiral phases. Ioffe and Larkin showed that quantum fluctuations necessarily lead to a development of a gapped spin-liquid phase in the vicinity of the Lifshitz point. A frustration by itinerant fermions is very different from that in nonitinerant systems. Nevertheless, in this paper we show that quantum fluctuations in the $t - J$ model in the vicinity of the classical Lifshitz point also lead to the spin-liquid phase due to the mechanism similar to that by Ioffe and Larkin. Hence, the classical
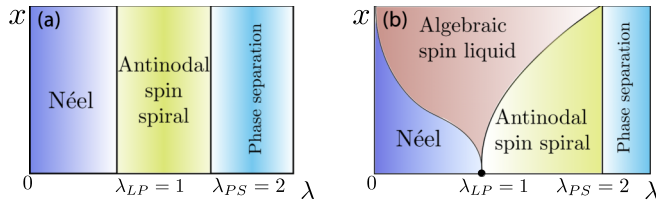
FIG. 1. Zero temperature phase diagram of a lightly doped extended $t - J$ model; x is hole doping, λ is an effective fermion-magnon coupling parameter. (a) Classical phase diagram [9]. (b) Quantum phase diagram. Strong quantum fluctuations in the vicinity of the Lifshitz point (λ_{LP}) result in a new algebraic spin-liquid phase.

Lifshitz line shown in Fig. 1(a) expands to a finite spin-liquid region shown in Fig. 1(b). The endpoint of the classical Lifshitz line at $x = 0$ becomes a quantum tricritical Lifshitz point.

In the present paper, we calculate the phase diagram, analyze properties of the spin-liquid phase, and compare our results with experimental observations for cuprates. We argue that cuprates belong to a relatively narrow vertical band near $\lambda \approx 1$ in the phase diagram Fig. 1(b). In our analysis, we consider the single-layer model in the absence of disorder. Therefore, our results are applicable to cuprates at doping $x \gtrsim 5\%$. At doping lower than 5%, the spin-spiral physics in LSCO is driven by disorder [13,14], and in YBCO the physics is driven by the bilayer character of the compound [15]. The spin liquid in the $t - J$ model, besides some similarities, has many differences from the Ioffe-Larkin spin liquid in frustrated magnets. The most noticeable qualitative differences are (i) magnetic response in the spin-liquid phase in the $t - J$ model has a finite spectral weight at low energies (magnetic pseudogap), in contrast to a fully gapped magnetic response in the Ioffe-Larkin case, and (ii) the decay of spin-spin correlation with the distance is different in the two cases. In the Ioffe-Larkin spin liquid, the correlator decays exponentially with distance [16]. On the other hand, in the $t - J$ model spin liquid is algebraic and the correlator decays as $1/r^3$.

Following Refs. [8,11], we rely on quantum field theory formalism. Interestingly, even experimental data indicates that the field theory is a very natural approach to the problem. In Fig. 2, we present magnetic dispersion along the (1,0) crystal axis taken from Ref. [17]. The figure shows combined data on resonant inelastic x-ray scattering and inelastic neutron scattering. The data demonstrates three distinct regimes separated in Fig. 2 by vertical lines. In the ultraviolet regime, the dispersion only very weakly depends on doping, practically doping independent. The independence is consistent with high temperature NMR data [18]. In the intermediate regime, there is a significant softening of the magnon dispersion with doping and the most dramatic doping dependence takes place in the infrared regime. We set the ultraviolet cutoff for the field theory $q \approx \Lambda_q$ that is the upper edge of the intermediate regime as shown in Fig. 2. The value of the cutoff indicated by the data is $\Lambda_q \sim 0.2$(r.l.u) $\sim 1.2/a$, where r.l.u. are reciprocal lattice units and $a = 3.81$ Å is the lattice spacing of the square CuO_2 plane. In the main text, we will determine the value of Λ_q theoretically and show that Λ_q
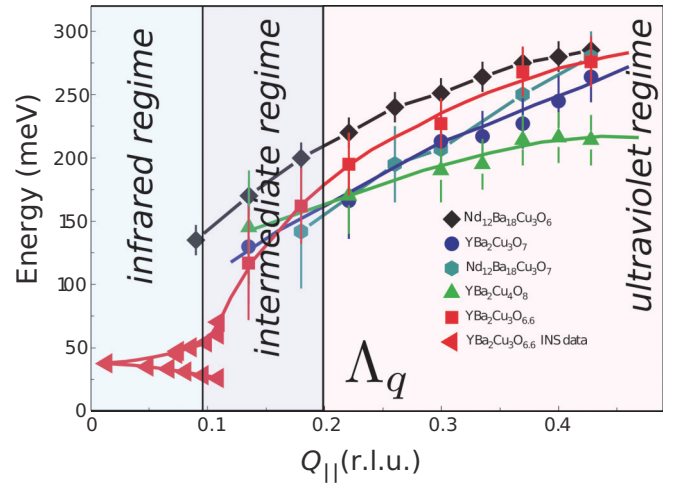

FIG. 2. Magnetic dispersion along the (1,0) direction. Points show combined data on resonant inelastic x-ray scattering and inelastic neutron scattering in NdBCO and YBCO at $T = 15$ K, Ref. [17]. Vertical lines separate three different regimes that we call infrared regime, intermediate regime, and ultraviolet regime.

is independent of doping. The spin-wave theory works well at $q > \Lambda_q$; moreover, in this regime the field theory is not valid and only the spin-wave theory is applicable. On the other hand, the magnon dispersion is linear in q at $q \lesssim \Lambda_q$ and this justifies applicability of the field theory. The crossover energy scale between the intermediate regime and the infrared regime depends on doping and the change of the regime is related to the energy E_{cross} discussed in the experimental review in Ref. [1]. We calculate values of E_{cross} for different values of doping and compare our results with data. In the low doping limit, $x \to 0$, the size of the "infrared" domain shrinks to zero. In our analysis, besides the already mentioned publications, we use some ideas from Refs. [19–22]. We would also like to mention a recent work, Ref. [23], where an emergence of topological order in the pseudogap phase was proposed. This is an interesting possibility; however, Ref. [23] does not consider magnetic excitations which are of primary interest in the present work.

The paper is organized as follows. In Sec. II, we review the procedure for the reduction of the extended $t - J$ model to the quantum field theory. The new point compared to already published results is the doping dependence of magnon speed. In Sec. III, we evaluate parameters of the field theory, calculate the dependence (reduction) of magnon speed on doping using self-consistent Born approximation (SCBA), and compare our predictions with inelastic neutron scattering data. In Sec. IV, we explain central ideas of the paper. Here we discuss the theory of the quantum Lifshitz transition driven by a coupling between spin excitations and low-energy fermionic modes. In the same section, we present a magnetic phase diagram and derive properties of the new spin-liquid phase. Here we separately consider a simple case of circular holon Fermi pockets and more realistic case of elliptic pockets. In Sec. V, we discuss the ultraviolet cutoff for the field theory and provide quantitative estimates for the "Lindemann criterion" of quantum melting. In the same section, we calculate E_{cross} and compare it with the experimental data. Furthermore, we
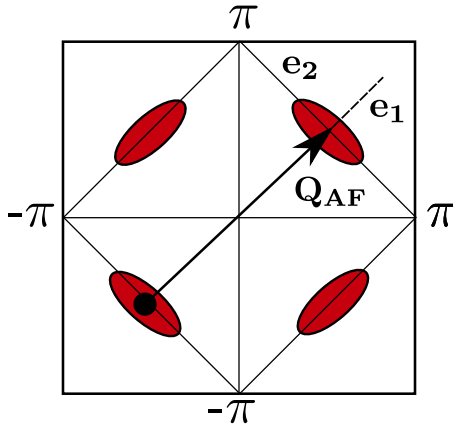
FIG. 3. Holon's Fermi pockets in underdoped cuprates.

numerically evaluate the phase boundaries in zero temperature phase diagram. In Sec. VI, we consider the equal time spin-spin correlator and demonstrate the algebraic decay. Finally, we summarize our results in Sec. VII.

II. LOW-ENERGY LIMIT OF THE EXTENDED $t - J$ MODEL: QUANTUM FIELD THEORY

The Hamiltonian of the extended $t - J$ model reads [5–7]

$$H = -t \sum_{\langle ij \rangle} c_{i,\sigma}^\dagger c_{j,\sigma} - t' \sum_{\langle\langle ij \rangle\rangle} c_{i,\sigma}^\dagger c_{j,\sigma}$$
$$- t'' \sum_{\langle\langle\langle ij \rangle\rangle\rangle} c_{i,\sigma}^\dagger c_{j,\sigma} + J \sum_{\langle i,j \rangle} \left[\boldsymbol{S}_i \cdot \boldsymbol{S}_j - \frac{1}{4} N_i N_j \right], \quad (1)$$

where $c_{i\sigma}^\dagger$ ($c_{i\sigma}$) is the creation (annihilation) operator for an electron with spin $\sigma = \uparrow, \downarrow$ at Cu site i; the operator of electron spin reads $\boldsymbol{S}_i = \frac{1}{2} c_{i\alpha}^\dagger \boldsymbol{\sigma}_{\alpha\beta} c_{i\beta}$. The electron number density operator is $N_i = \sum_\sigma c_{i\sigma}^\dagger c_{i\sigma}$, where x is the hole doping, so that the sum rule $\langle N_i \rangle = 1 - x$ is obeyed. In addition to Hamiltonian Eq. (1), there is the no double occupancy constraint, which accounts for a strong electron-electron on-site repulsion. Values of parameters slightly vary between different compounds. Typically, $J \approx 125\,\text{meV}$ and the hopping integrals are $t \approx 390\,\text{meV} \approx 3J$, $t' \approx 90$ meV $\approx -0.7J$, and $t'' \approx 80$ meV $\approx 0.6J$, see, e.g., Ref. [24] The Fermi surface of a lightly doped extended $t - J$ model consists of Fermi pockets shown in Fig. 3 and centered at the nodal points $\mathbf{k}_0 = (\pm\pi/2, \pm\pi/2)$ and $\mathbf{k}_0 = (\pm\pi/2, \mp\pi/2)$. The hole dispersion can be approximately calculated using SCBA, that is well known to be very reliable for the single hole problem in the $t - J$ model. The single hole dispersion can be parametrized as [25]

$$\epsilon_{\boldsymbol{k}} = \beta_1 (\gamma_{\boldsymbol{k}}^+)^2 + \beta_2 (\gamma_{\boldsymbol{k}}^-)^2, \quad \gamma_{\boldsymbol{k}}^\pm = \frac{1}{2}(\cos k_x \pm \cos k_y),$$

$$\epsilon_{\boldsymbol{k}} \approx \beta_1 \frac{p_1^2}{2} + \beta_2 \frac{p_2^2}{2}. \quad (2)$$

Hereafter we set the lattice spacing equal to unity, $a = 3.81\,\text{Å} \to 1$. The second line in Eqs. (2) corresponds to the quadratic expansion of the fermion dispersion along the principle axes of the Fermi surface ellipse, Fig. 3, $\mathbf{p} = \mathbf{k} - \mathbf{k}_0$, and

Fermi energy is related to doping as

$$\epsilon_F \approx \pi\beta x,$$

$$\beta = \sqrt{\beta_1 \beta_2} = \frac{1}{m^*}. \quad (3)$$

Inverse effective masses β_1, β_2 can be calculated within the extended $t - J$ model in SCBA approximation and they significantly depend on t' and t'', see Ref. [10]. At values of t' and t'', corresponding to cuprates, the inverse effective mass is $2J < \sqrt{\beta_1 \beta_2} < 2.5J$. Hence, the effective mass of a hole is approximately twice the electron mass, $m^* \approx 2m_e$.

While the $t - J$ model is the low energy reduction of the three band Hubbard model, the total energy range in the $t - J$ model, $\Delta\epsilon \sim 8t \sim 2J \approx 3$ eV, is still very large. On the other hand, we are interested in the energy interval bounded by the top edge of the intermediate regime in Fig. 2, $E \lesssim 150-200$ meV. Therefore, for our purposes, it is quite natural to consider the low-energy sector of $t - J$ model. The effective low-energy Lagrangian was first derived in Ref. [8] with some important terms responsible for stability of the spin-spiral ground state missing. The full effective Lagrangian was derived in Ref. [11]. This approach necessarily requires an introduction of two checkerboard sublattices, independent of whether there is a long-range AFM order or the order does not exist. The two checkerboard sublattices allow us to avoid a double counting of quantum states in the case when spin and charge are separated. A hole, which hereafter we call a holon, does not carry a spin, but it can be located at one of the sublattices and this is described by the pseudospin $1/2$. Due to the checkerboard sublattices the Brillouin zone coincides with magnetic Brillouin zone (MBZ) even in the absence of a long-range AFM order. Therefore, there are four half-pockets in Fig. 3 or two full pockets within MBZ. Finally, the Lagrangian reads [11]

$$\mathcal{L} = \frac{\chi_\perp}{2} \dot{\vec{n}}^2 - \frac{\rho_s}{2} (\nabla\vec{n})^2 + \sum_\alpha \left\{ \frac{i}{2} [\psi_\alpha^\dagger \mathcal{D}_t \psi_\alpha - (\mathcal{D}_t \psi_\alpha)^\dagger \psi_\alpha] \right.$$
$$\left. - \psi_\alpha^\dagger \epsilon_\alpha(\mathcal{P})\psi_\alpha + \sqrt{2}g(\psi_\alpha^\dagger \vec{\sigma}\psi_\alpha) \cdot [\vec{n} \times (\boldsymbol{e}_\alpha \cdot \nabla)\vec{n}] \right\}. \quad (4)$$

Fermions (holons) are described by a spinor ψ_α with the pseudospin $1/2$, and the vector of staggered magnetization $\boldsymbol{n}$ normalized as $\boldsymbol{n}^2 = 1$ corresponds to localized spins at Cu sites. The first line in Eq. (4) is $O(3)$ nonlinear sigma model that describes spin dynamics, the second line is the Lagrangian for noninteracting holons. The long covariant derivatives in Eq. (4) are defined as

$$\boldsymbol{P} = -i\nabla + \frac{1}{2}\vec{\sigma} \cdot [\vec{n} \times \nabla\vec{n}], \quad (5)$$

$$\mathcal{D}_t = \partial_t + \frac{1}{2}\vec{\sigma} \cdot [\vec{n} \times \partial_t \vec{n}]. \quad (6)$$

The index $\alpha = 1, 2$ enumerates two full holon pockets in Fig. 3. The term in the bottom line in Eq. (4) describes a coupling between holons and the staggered magnetization. Pauli matrices $\boldsymbol{\sigma}$ in Eq. (4) act on the holon's pseudospin and $\boldsymbol{e}_\alpha = 1/\sqrt{2}(1, \pm 1)$ denotes a unit vector orthogonal to the face of the MBZ where the holon is located.

Lagrangian Eq. (4) contains five parameters, $\chi_\perp, \rho_s, \beta_1, \beta_2$, and g. Parameters of a quantum field theory always depend

on the energy/momentum scale and hence the values of the parameters are fixed at a particular normalization point. We use the ultraviolet limit Λ_q discussed in the Introduction as the normalization point. In the limit $x \to 0$, the σ-model parameters $\chi_\perp$ and ρ_s coincide with that of the 2D Heisenberg model on the square lattice, $\chi_\perp = 1/8J$, $\rho_s = J/4$ and the magnon speed

$$c_0 = \sqrt{\rho_s/\chi_\perp} = \sqrt{2}\, J. \tag{7}$$

The coupling constant is $g = Zt$, where Z is the holon quasiparticle residue calculated within the $t - J$ model [25]. For t' and t'' corresponding to cuprates and even for $t' = t'' = 0$, the coupling constant is always close to $g \approx J$.

The most important parameter that drives magnetic quantum criticality in the model is the effective fermion-magnon coupling strength [11]

$$\lambda = \frac{2g^2}{\pi \rho_s \sqrt{\beta_1 \beta_2}}. \tag{8}$$

Lagrangian Eq. (4) has been analyzed previously in a classical mean-field approximation. The phase diagram obtained in this approximation is shown in Fig. 1(a). The collinear AFM state is stable at $\lambda < 1$. At $\lambda > 1$, the spin spiral is developing, the wave vector of the spiral depends linearly on doping, $Q \propto x$, Ref. [8] The direction of the spiral wave vector is antinodal, i.e., $\mathbf{Q} \propto (1, 0)$ or $\mathbf{Q} \propto (0, 1)$ and at further increasing of λ a phase separation instability is developing at $\lambda_{PS} = 2$, Refs. [9,11]. Taking the values of the field theory parameters corresponding to cuprates, as described in the previous paragraph, the value of λ is $1 < \lambda < 1.3$ [26]. In theory, one can vary λ arbitrarily. For example, in the pure $t - J$ model, $t' = t'' = 0$, the value of β_2 is very small and hence $\lambda > 2$, the model is unstable with respect to the phase separation [27]. Within the extended $t - J$ model it is rather hard to make λ significantly smaller than 1. For instance, using the set of the $t - J$ model parameters with an unreasonably high value of t'', $t = 3J$, $t' = 0$, $t'' = 3J$, the SCBA approximation gives $\lambda \approx 0.7$. This set of parameters is unphysical. For realistic parameters of cuprates, λ is close to unity and probably slightly higher than unity. We estimate the interval for the parameters of cuprates as

$$0.9 < \lambda < 1.3. \tag{9}$$

While there is no experimentally available handle that would allow one to directly tune parameter λ in a given cuprate compound, parameter λ is vital for the description of phase transitions between different magnetic states in cuprates.

III. SOFTENING OF MAGNONS IN THE "INTERMEDIATE" REGIME

Softening of magnons with doping in cuprates was observed in inelastic neutron scattering a long time ago, see Refs. [28–30], see also an experimental review in Ref. [1]. This phenomenon still lacks a theoretical explanation. In this section, we calculate the dependence of the field theory parameters on doping and, as a byproduct of this analysis, we explain the softening. The physics discussed in the present section concerns relatively high energies and it is independent
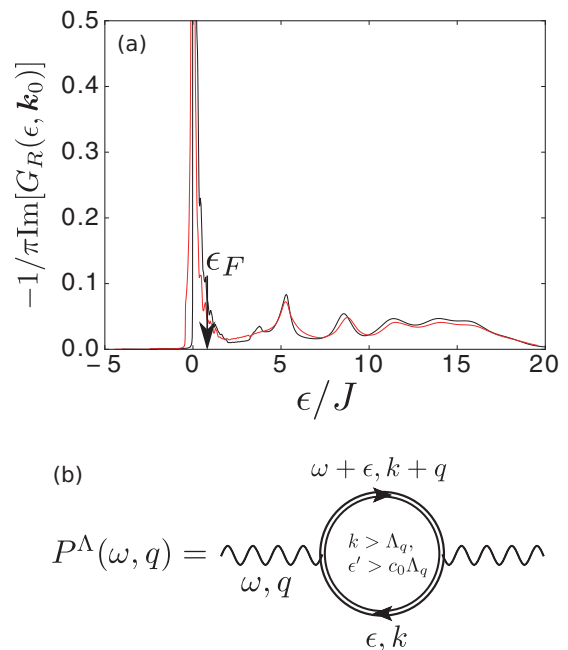

FIG. 4. (a) Spectral density of holon's retarded Green's function at $\mathbf{k_0} = (\pi/2, \pi/2)$ calculated [25] numerically in SCBA. The black line corresponds to the set of parameters $t = 3.1J$, $t' = -0.5J$, $t'' = 0.4J$, and the red line corresponds to $t = 3.1J$, $t' = -0.8J$, $t'' = 0.7J$. The arrow shows the value of the Fermi energy for the doping interval $5\% \leqslant x \leqslant 15\%$. (b) Magnon polarization operator $P^\Lambda(\omega, \mathbf{q})$, the double line represents dressed holon Feynman Green's function.

of the Lifshitz magnetic criticality that is driven by λ and is discussed in subsequent sections.

The single hole problem in the $t - J$ model was solved decades ago using SCBA, and we will skip all technical details of such calculations. The spectral density of a single holon retarded Green's function,

$$G_R(\epsilon, \mathbf{k}) = -i \int dt\, d\mathbf{r}\, e^{-i\epsilon t + i\mathbf{kr}} \langle T\{c_\uparrow^\dagger(\mathbf{r}, t)c_\uparrow(0, 0)\}\rangle, \tag{10}$$

is plotted in Fig. 4(a). The spectral density can be represented as

$$-\frac{1}{\pi} Im[G_R(\epsilon, \mathbf{k})] = Z_{\mathbf{k}} \delta(\epsilon - \epsilon_{\mathbf{k}}) + \rho_{\mathbf{k}}(\epsilon). \tag{11}$$

Here $Z_{\mathbf{k}}$ is the holon's quasiparticle residue, $\epsilon_{\mathbf{k}}$ is the holon's dispersion Eqs. (2), and $\rho_{\mathbf{k}}$ is the the incoherent "tail." The incoherent part of the retarded holon's Green's function vanishes below the Fermi energy, $\epsilon < \epsilon_F$, see Fig. 4(a). The incoherent tail stretches up to very high energies and is equal to the energy span of the $t - J$ model $\Delta\epsilon \sim 8t \sim 24J \approx 3$ eV. At small doping, the spectral density of Feynman Green's function can be expressed in terms of Eq. (11), Ref. [31]

$$-\frac{1}{\pi} Im[G_F(\epsilon, \mathbf{k})] = \text{sgn}(\epsilon - \epsilon_F) Z_{\mathbf{k}} \delta(\epsilon - \epsilon_{\mathbf{k}}) + \rho_{\mathbf{k}}(\epsilon), \tag{12}$$

where $\text{sgn}(z) = z/|z|$ and ϵ_F is Fermi energy Eqs. (3). The incoherent spectral density has positive, $\rho^{(+)}$, and negative, $\rho^{(-)}$, frequency parts.

The magnon polarization operator $P^\Lambda(\omega, \mathbf{q})$ is given by the fermionic loop shown in Fig. 4(b). The magnon Green's function defined on the local AFM background directed along the z axis reads

$$\vec{n}_\perp = (n_x, n_y, 0),$$
$$\vec{n} = (n_x, n_y, \sqrt{1 - n_\perp^2}),$$
$$D(t, \mathbf{r})\delta_{\alpha\beta} = -i\langle T\{n_{\perp,\alpha}(t, \mathbf{r})n_{\perp,\beta}(0, 0)\}\rangle. \quad (13)$$

The standard expression for magnon Green's function in a single loop approximation reads $D(\omega, \mathbf{q}) = \chi_\perp^{-1}[\omega^2 - c^2\mathbf{q}^2 - P(\omega, \mathbf{q}) + i0]^{-1}$. In what follows, we will separately consider the magnon's Green's function in the two regimes corresponding to the two energy/momentum scales. (i) Ultraviolet scale, $q \sim \Lambda_q \approx 1$, $\omega \sim c_0\Lambda_q \sim J \sim 200$ meV, where all slow fluctuations related to magnetic criticality are irrelevant. In this regime, the magnon's propagator is

$$D^\Lambda(\omega, \mathbf{q}) = \frac{\chi_\perp^{-1}}{\omega^2 - c_0^2\mathbf{q}^2 - P^\Lambda(\omega, \mathbf{q}) + i0}, \quad (14)$$

where we use the "bare" magnon speed $c_0 = \sqrt{2}J$ and the polarization operator P^Λ is shown in Fig. 4(b). In this regime, in the polarization bubble $P^\Lambda(\omega, \mathbf{q})$ only high energy particle-hole excitations with energies $|\epsilon_k - \epsilon_F| \gg \Lambda$ are accounted, that is emphasized by the superscript Λ. As we demonstrate in the present section, the polarization operator P^Λ is responsible for the reduction of the magnon speed with doping. The second energy scale corresponds to (ii) intermediate $+$ infared regimes, which are presented in Fig. 2. The physics in the case (ii) is related to magnetic criticality, and will be addressed in following sections. The information about the ultraviolet physics is incorporated in the low-energy physics (ii) via renormalized parameters of the Lagrangian (e.g., renormalized magnon speed c).

The fermion loop diagram P^Λ, shown in Fig. 4(b), contains a product of the positive and negative frequency components of the fermion Feynman Green's function Eq. (12). There are four contributions to the polarization operator: (i) coherent-coherent $P^{(cc)} \propto Z_k Z_{k+q}$ ($k < p_F$, $|\mathbf{k} + \mathbf{q}| > p_F$), (ii) coherent-incoherent $P^{(ci)} \propto Z_k \rho_{k+q}^{(+)}$ ($k < p_F$, $|\mathbf{k} + \mathbf{q}|$ is arbitrary), (iii) incoherent-incoherent $P^{(ii)} \propto \rho_k^{(-)}\rho_{k+q}^{(+)}$ (both k and $|\mathbf{k} + \mathbf{q}|$ are arbitrary), (iv) incoherent-coherent $P^{(ic)} \propto \rho_k^{(-)}Z_{k+q}$ (k is arbitrary, $|\mathbf{k} + \mathbf{q}| > p_F$).

(i) The coherent-coherent contribution, $P^{(cc)}$, is responsible for the quantum critical physics in the infared regime and actually it cannot be accurately calculated within the "simplistic" logic of this section, where we consider only the high energy behavior. The physics in the infared regime, $\omega \sim \epsilon_F$, where $P^{(cc)}$ plays the central role will be considered in the next section. Here it is sufficient to estimate $P^{(cc)}$ at energy equal to our ultraviolet limit, $\omega \sim c_0\Lambda_q \gg \epsilon_F$. A straightforward calculation similar to that performed in the

next section gives

$$P^{(cc)} \sim -8J^2xq^2\left(\frac{\beta q^2}{\omega^2}\right). \quad (15)$$

(ii) The coherent-incoherent contribution reads

$$P^{(ci)}(\omega, \mathbf{q}) \approx 4\sum_{\alpha=1,2}\int_{k<p_F}\frac{d^2k}{(2\pi)^2}(\tilde{g}_{\mathbf{k},\mathbf{q}})^2$$
$$\times \int_{c_0\Lambda_q}^\infty dy \frac{Z_\mathbf{k}\rho_{\mathbf{k}+\mathbf{q}}^{(+)}(y)}{\omega - \epsilon_\mathbf{k}^\alpha - y}. \quad (16)$$

Here α enumerates holon pockets, and the the holon-magnon vertex $\tilde{g}_{\mathbf{k},\mathbf{q}}$ is related to $g_{\mathbf{k},\mathbf{q}}$ from Ref. [25] as

$$\tilde{g}_{\mathbf{k},\mathbf{q}} = \sqrt{2\omega_q}g_{\mathbf{k},\mathbf{q}} = 4\sqrt{2}t\sqrt{2\omega_q}(\gamma_\mathbf{k}u_\mathbf{q} + \gamma_{\mathbf{k}+\mathbf{q}}v_\mathbf{q}). \quad (17)$$

The factor $\sqrt{2\omega_q}$ in the vertex $\tilde{g}_{\mathbf{k},\mathbf{q}}$ is due to a normalization. Here we use the standard quantum field theory normalization for the magnon field while Ref. [25] has used the Schrödinger equation normalization. In the vicinity of a given Fermi pocket, $\mathbf{k} \approx \mathbf{k}_0 = (\pi/2, \pm\pi/2)$ and at $q < 1$ the vertex Eq. (17) reads

$$\tilde{g}_{\mathbf{k},\mathbf{q}} \approx 4t\sqrt{2J}q_{1,\alpha}, \quad (18)$$

where $q_{1,\alpha}$ is the component of the momentum orthogonal to the face of the MBZ in this pocket.

The incoherent component of the holon's Green's function remains approximately constant $\rho^{(+)}(y) \approx (1 - Z_k)/8t$ in the energy interval $2J \lesssim \epsilon \lesssim 8t$, see Fig. 4(a). The latter estimate for the incoherent part of the holon's spectral function follows from the approximate sum rule $Z_k + \int_0^{+\infty} d\omega\rho_k^{(+)}(\omega) \approx 1$. We also set $Z_k = J/t$. Hence, from Eq. (16) and Eq. (18) we find

$$P^{(ci)}(\mathbf{q}) \approx -32t^2q^2\left(J\int_{2J}^\infty \frac{\rho(y)}{y}dy\right)\left[4\int_{k<p_F}\frac{d^2k}{(2\pi)^2}Z_\mathbf{k}\right]$$
$$\approx -32t^2x\, q^2 Z_{\mathbf{k}_0}\left(J\int_{2J}^\infty \frac{\rho(y)}{y}dy\right)$$
$$\approx -4xJ^2q^2\left(1 - \frac{J}{t}\right)\ln\left(\frac{4t}{J}\right). \quad (19)$$

The integral in this formula converges at very high energies, $y \sim 8t$, much higher than the ultraviolet cutoff of the field theory. This is why calculation of $P^{(ci)}$, Eq. (19) is accurate, while $P^{(cc)}$, Eq. (15), is only an estimation. At the ultraviolet cutoff $\omega = c_0\Lambda_q \approx 200$ meV $\gg \epsilon_F$ the coherent-coherent contribution, Eq. (15), is negligible compared to $P^{(ci)}$ given by Eq. (19).

(iii) Unfortunately, the incoherent-incoherent contribution, $P^{(ii)}$, arising from $\rho_k^{(-)}\rho_{k+q}^{(+)}$ cannot be calculated analytically. Fortunately, this contribution is relatively small, in Ref. [31] it was estimated numerically as 20–25% of $P^{(ci)}$. It has the same scaling as $P^{(ci)}$, $P^{(ii)} \propto J^2xq^2$. The smallness of $P^{(ii)}$ compared to $P^{(ci)}$ is related to the smalness of $\rho^{(-)}$, see Fig. 4 in Ref. [32].

(iv) The incoherent-coherent contribution, $P^{(ic)}$, scales approximately as Eq. (15) and is very small due to the same reasons as that presented in (iii), Refs. [31,32].
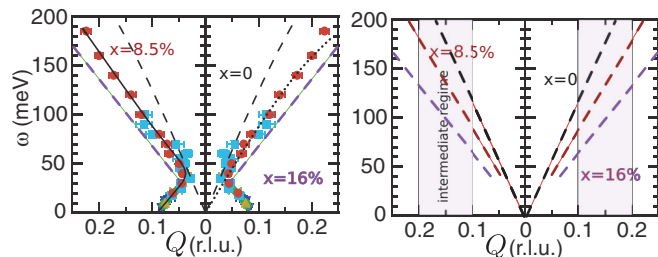
FIG. 5. Magnon dispersion in the intermediate regime, 70 meV $< \omega <$ 200 meV, Left panel presents experimental data for $x = 0$ (Ref. [33]), $x = 0.085$ (Ref. [29]), and $x = 0.16$ (Ref. [30]) (black, red, and magenta dashed lines, respectively). Right panel: Theoretical magnon dispersion Eq. (23) for the same values of doping. Shaded regions indicate the "intermediate regime" where the right and the left panels should be compared.

All in all P^Λ is given by Eq. (19). To account for $P^{(ii)}$ contribution, we multiply Eq. (19) by an additional factor ~ 1.25, that gives for $t/J \approx 3$ the following approximate result:

$$P^\Lambda(\mathbf{q}) \approx -8J^2 q^2 x. \tag{20}$$

Hence the magnon Green's function Eq. (14) reads

$$D^\Lambda(\omega, q) = \frac{\chi_\perp^{-1}}{\omega^2 - c_0^2(1 - 4x)q^2 + i0}. \tag{21}$$

Note that only the coefficient in front of q^2 is changing with doping, the ω-term is not changed since the doping correction comes from very high energy fluctuations, $8t \gg \omega$. From Eq. (21) we deduce parameters of the effective nonlinear σ-model in the Lagrangian Eq. (4):

$$\chi_\perp = \chi_\perp^{(0)} = 1/8J,$$

$$\rho_s = \rho_s^{(0)}(1 - 4x) = \frac{J}{4}(1 - 4x). \tag{22}$$

Hence the magnon speed is reduced with the doping:

$$c = \sqrt{\frac{\rho_s}{\chi_\perp}} = c_0\sqrt{1 - 4x}. \tag{23}$$

Softening of magnons in the energy interval 70 meV $< \omega <$ 200 meV which we call the intermediate regime was observed in inelastic neutron scattering [28–30]. To illustrate this in the left panel of Fig. 5, we present data for LSCO from Refs. [29,30,33] for doping levels $x = 0$, $x = 0.085$, and $x = 0.16$. In the right panel of Fig. 5, we plot the theoretical dispersion Eq. (23) for the same values of doping. The agreement between theory and experiment in the intermediate regime is remarkable even at $x = 0.16$ where the spin-wave velocity reduction is approximately 40%.

Physics that we have discussed in the present section concerns relatively high energies and it is irrelevant to Lifshitz point magnetic criticality. So, the doping dependence presented in Eqs. (22) and (23) is only weakly sensitive to λ. In the interval Eq. (9) it is practically λ-independent.

We have calculated the doing dependence of $c(x)$ and $\rho_s(x)$. What can we say about doping dependence of other parameters of the Lagrangian Eq. (4)? Inverse effective masses β_1 and β_2 are slightly dependent on doping. The doping

increases β_1 and decreases β_2 in such a way that the average effective inverse mass $\beta = \sqrt{\beta_1\beta_2}$ is approximately doping independent [27]. Here we disregard the weak doping dependence of β_1 and β_2. On the other hand, doping dependence of the coupling constant g is expected to be significant. Due to the magnon softening Eq. (23) the coupling constant g must be decreasing with doping. Unfortunately, we do not know how to perform a reliable calculation of the coupling constant reduction with doping. In what follows, we will expect that g varies with doping in such a way that the magnetic criticality parameter λ defined by Eq. (8) is approximately doping independent.

IV. MAGNETIC CRITICALITY AT THE LIFSHITZ POINT AND THE SPIN LIQUID PHASE

We start our analysis of the low-energy infrared regime + intermediate regime from the usual collinear AFM state. The staggered magnetization is directed along the z axis and we use the standard representation Eq. (14). The dynamics is described by the effective Lagrangian Eq. (4). To explain our idea, we first consider circular Fermi pockets and then consider ellipticity of the pockets. This is a conceptual section, so we derive general equations, but perform specific calculations only for very small doping x where the calculations can be done analytically with logarithmic accuracy.

A. Circular Fermi pockets, $\beta = \beta_1 = \beta_2$

The magnon Green's function reads

$$D(|\omega| < \Lambda, q < \Lambda_q) = \frac{\chi_\perp^{-1}}{\omega^2 - c^2 q^2 - P^F(\omega, \mathbf{q}) + i0}, \tag{24}$$

Formally this equation is similar to Eq. (14), and the polarization operator is given by the standard loop diagram, as shown in Fig. 4(b). However, there are two important differences. (i) Unlike Eq. (14), which contains the bare magnon speed c_0, Eq. (24) contains the renormalized magnon speed c given by Eq. (23). (ii) Equation (14) contains the ultraviolet polarization operator P^Λ which results mainly from the coherent-incoherent contribution and from the energy scale up to $24J \sim 3$ eV. On the other hand, Eq. (24) contains the coherent-coherent polarization operator P^F, which is relevant at the energy scale $\epsilon \sim \epsilon_F \sim 20 - 50$ meV. We would like to emphasize again the point explained in the previous section: although the coherent-coherent contribution [see Eq. (26)] is crucial for the infrared physics, it is suppressed in the high energy regime $\omega \sim J \sim \Lambda \gg \epsilon_F$ by the parameter $\mathcal{O}(\epsilon_F^2/\omega^2)$, Eq. (15). To further clarify our method, we can say that we perform a sort of "two-step" renormalization group procedure: we first calculate correction to the magnon velocity at the intermediate energy scale and then use the result to evaluate polarization operator at the infrared energy scale.

The normalization point of our field theory is $q = \Lambda_q$, $\omega = c_0\Lambda_q$. At the normalization point $\vec{n} = (0, 0, 1)$, i.e., $\vec{n}_\perp = 0$. The quantum transversal fluctuation (we assume zero temperature) of the staggered magnetization at $q = \omega = 0$

reads

$$\langle \vec{n}_\perp^2 \rangle = -2 \sum_{q < \Lambda_q} \int_{|\omega| < c_0 \Lambda_q} \frac{d\omega}{2\pi i} \, D(\omega, \boldsymbol{q}) . \qquad (25)$$

The factor 2 comes from summation over magnon transverse polarizations. The magnon polarization operator P^F reads (see Ref. [11])

$$P^F(\omega, \boldsymbol{q}) = \frac{2}{\chi_\perp} \sum_{k, \alpha} f_k^\alpha \left(1 - f_{k+q}^\alpha\right) \frac{[\sqrt{2} g(\boldsymbol{e}_\alpha \cdot \boldsymbol{q})]^2}{\omega + \epsilon_k^\alpha - \epsilon_{k+q}^\alpha + i0}$$
$$+ \{\omega \to -\omega, \, \boldsymbol{q} \to -\boldsymbol{q}\}. \qquad (26)$$

Here $f_k^\alpha = \theta(\epsilon_F - \epsilon_k^\alpha)$ denotes the zero temperature Fermi-Dirac distribution for holons in the pocket α. The expression in the brackets [...] is the fermion-magnon vertex that follows from the bottom line in Lagrangian Eq. (4). Equation (26) up to the prefactor is the usual 2D Lindhard Function. The prefactor $\propto \boldsymbol{q}^2$ is dictated by the Adler's theorem. After the Wick rotation from real to imaginary frequency, $\omega = i\xi$, the polarization operator reads

$$P^F(i\xi, \boldsymbol{q}) = -\lambda c^2 q^2 \left(1 - \frac{2}{q^2} \text{Re} \sqrt{\left(\frac{q^2}{2} + i\frac{\xi}{\beta}\right)^2 - p_F^2 q^2}\right). \qquad (27)$$

Here we assume quadratic holon dispersion, $\epsilon_k^\alpha = \beta \boldsymbol{p}^2/2$ ($\boldsymbol{p} = \boldsymbol{k} - \boldsymbol{k}_0^\alpha$), the Fermi momentum is $p_F = \sqrt{\pi x}$. Since natural scales in Eq. (27) are ϵ_F and p_F, it is convenient to express the polarization operator in terms of dimensionless energy and momentum

$$\tilde{q} = \frac{q}{p_F}, \quad \tilde{\xi} = \frac{\xi}{\epsilon_F} . \qquad (28)$$

Hence the quantum fluctuation Eq. (25) reads

$$\langle \vec{n}_\perp^2 \rangle = \frac{\beta x}{2\pi \rho_s} \int_0^{\Lambda/p_F} d\tilde{q} \, F(\tilde{q}), \qquad (29)$$

$$F(\tilde{q}) = \tilde{q} \int_0^{c\Lambda/\epsilon_F} \frac{d\tilde{\xi}}{\gamma \tilde{\xi}^2 + \tilde{q}^2(1 - \lambda r)}, \qquad (30)$$

where $\gamma = \frac{\pi \beta^2}{4c^2} x \ll 1$ and

$$r = \text{Re} \left\{ 1 - \frac{1}{\tilde{q}^2} \sqrt{(\tilde{q}^2 + i\tilde{\xi})^2 - 4\tilde{q}^2} \right\}. \qquad (31)$$

We consider the collinear phase, hence $\lambda < 1$. The central point is that the integral Eq. (29) is logarithmically diverging in the limit $\lambda \to 1$. The main contribution to the integral comes from very small ξ where the function r in Eq. (31) can be expanded as

$$r \approx 1 - \frac{|\tilde{\xi}|}{\tilde{q} \sqrt{4 - \tilde{q}^2}}. \qquad (32)$$

Evaluation of the $\tilde{\xi}$ integral in Eq. (30) results in

$$F(\tilde{q}) = \theta(4 - \tilde{q}^2) \sqrt{4 - \tilde{q}^2} \ln\left(\frac{1}{1 - \lambda}\right) + f(\tilde{q}), \qquad (33)$$

where $f(\tilde{q})$ only weakly depends on λ. The $\tilde{q}$-integration in Eq. (29) is straightforward

$$\langle \vec{n}_\perp^2 \rangle = \frac{\beta x}{2\rho_s} \ln\left(\frac{1}{1 - \lambda}\right) + \phi(\lambda, \gamma), \qquad (34)$$

where again $\phi(\lambda, \gamma)$ is nonsingular and only weakly depends on λ near $\lambda \approx 1$. In the limit $x \to 0$, we should recover the result for the 2D Heisenberg model, hence $\langle \vec{n}_\perp^2 \rangle = \phi(\gamma \to 0, \lambda) \approx 0.8$. In the rest of the section, we will assume that $\phi(\gamma, \lambda) \approx \phi$ is approximately constant. The logarithmic singularity in Eq. (34) at $\lambda \to \lambda_{\text{LP}} = 1$ is of central importance. The singularity indicates an instability of the AFM state when λ is sufficiently close to unity. The singularity is similar to the logarithmic divergence of transversal spin fluctuations in Ioffe-Larkin at the Lifshitz point in frustrated magnets [12,16]. In addition, the singularity is also analogous to the logarithmic divergence in 2D Heisenberg model at finite temperature [34]. The doping x in this case plays a role of an effective temperature. The divergence indicates the quantum phase transition to the disordered spin liquid phase.

There is a critical value of the fluctuation

$$\langle \vec{n}_\perp^2 \rangle_c \sim 1 \qquad (35)$$

that is sufficient to destroy the long-range AFM order. This is a sort of Lindemann criterion for quantum melting. We will discuss value of $\langle \vec{n}_\perp^2 \rangle_c$ later. Now we consider the problem conceptually. To find the critical value $\lambda_{c1} < 1$ for transition to the spin-liquid phase, we only need to equate the right-hand side of Eq. (34) to $\langle \vec{n}_\perp^2 \rangle_c$. This gives

$$1 - \lambda_{c1} \propto \exp\left[-\frac{2\rho_s(\langle \vec{n}_\perp^2 \rangle_c - \phi)}{\beta x}\right]. \qquad (36)$$

Formula Eq. (36) determines the left boundary on the phase diagram Fig. 1(b). Note that Eq. (36) is valid only at very small x. For realistic x, one needs a numerical calculation performed later.

In the spin-liquid phase at $\lambda > \lambda_{c1}$, the magnon gap Δ is opened [12,16] and hence the Green's function Eq. (24) is transformed to

$$D(i\xi, \boldsymbol{q}) = -\frac{\chi_\perp^{-1}}{\xi^2 + c^2 q^2 + \Delta^2 + P^F(i\xi, \boldsymbol{q})}. \qquad (37)$$

In essence, Δ is the Lagrange multiplier $\mathcal{L} \to \mathcal{L} + \Delta^2(\vec{n}_\perp^2 - \langle \vec{n}_\perp^2 \rangle_c)$ that has to be determined from the condition

$$\langle \vec{n}_\perp^2 \rangle_c = 2 \sum_{|\boldsymbol{q}| < \Lambda_q} \int_{|\xi| \leqslant c\Lambda_q} \frac{d\xi}{2\pi} \frac{\chi_\perp^{-1}}{\xi^2 + c^2 \boldsymbol{q}^2 + \Delta^2 + P^F(i\xi, \boldsymbol{q})}. \qquad (38)$$

By construction, the gap Δ vanishes at $\lambda = \lambda_{c1}$.

It is instructive to calculate Δ exactly at the Lifshitz point, $\lambda = 1$. Performing calculations by analogy with Eqs. (29)–(34), one finds with logarithmic accuracy

$$\Delta_{\lambda=1}(x) \propto \exp\left[-\frac{\rho_s(\langle \vec{n}_\perp^2 \rangle_c - \phi)}{\beta x}\right]. \qquad (39)$$

We stress again that here we assume the limit of very small x. For realistic x, we will perform numerical calculation in Sec. V.

Now we consider the case $\lambda > 1$. At at a fixed doping x and at a sufficiently large $\lambda = \lambda_{c2} > 1$ the spin-liquid phase becomes unstable toward condensation of static spin spiral, see phase diagram in Fig. 2(b). The instability manifests as a pole in the Green's function Eq. (37) at $\xi = 0$. At $\xi = 0$ the denominator in Eq. (37) is

$$D^{-1}(0, q) \propto \Delta^2 + c^2 q^2 \left[1 - \lambda \left(1 - \mathrm{Re} \sqrt{q^2 - 4p_F^2} \right) \right]. \quad (40)$$

The inverse propagator has a minimum at $q = 2p_F$. Hence the instability of the spin liquid with respect to the static spin-spiral condensation is determined from the condition that the denominator of the magnon propagator equal to zero at $q = 2p_F$,

$$\Delta^2 - 4c^2 p_F^2 (\lambda - 1) = 0. \quad (41)$$

The critical line λ_{c2} can be found by solving Eq. (41) together with Eq. (38). Solving these equations in logarithmic approximation at very small x we find

$$\lambda_{c2} - 1 \propto \exp \left(-\frac{2\rho_s (\langle \vec{n}_\perp^2 \rangle_c - \phi)}{\beta x} \right). \quad (42)$$

There are three points to note. (i) While Δ is zero at the left borderline of the spin-liquid phase, $\lambda = \lambda_{c1}$, the gap is nonzero at the right borderline $\lambda = \lambda_{c2}$, see Fig. 2(b). However, in this case, Δ is not the real magnon gap, the magnetic pseudogap corresponds to the distance from the real ω-axis to the nearest pole in magnon's Green's function. Since at the phase boundary λ_{c2} the magnon's Green's function acquires a pole at zero frequency, the spin excitation gap is zero in agreement with the Goldstone theorem. (ii) At $\lambda > \lambda_{c2}$, the static spin-spiral with the wave vector $Q = 2p_F$ condenses

$$\vec{n} = A[\vec{e}_1 \cos(\mathbf{Q} \cdot \mathbf{r}) + \vec{e}_2 \sin(\mathbf{Q} \cdot \mathbf{r})]. \quad (43)$$

Close to the phase transition line the amplitude A is very small. (iii) Direction of the spiral wave vector $\mathbf{Q}$ can be arbitrary. This is because for circular Fermi pockets considered in this subsection our field theory "does not know" about the lattice orientation.

B. Elliptic Fermi pockets

To describe a situation relevant to cuprates, we consider elliptic Fermi pockets stretched along the face of the MBZ, see Fig. 3. We still use the parabolic approximation, the second line in Eqs. (2), $\beta_1 > \beta_2$. The magnon polarization operator in the case of elliptic pockets could be obtained from Eq. (27) by performing rescaling of $q_{1,2}$ in Eq. (26). Hence the dimensionless polarization operator $r(i\xi, \mathbf{q})$ in Eqs. (30) and (32) should be replaced by

$$q^2 \lambda r \rightarrow \lambda (q_1^2 r_a + q_2^2 r_b) = \lambda p_F^2 (\tilde{q}_1^2 r_a + \tilde{q}_2^2 r_b),$$

$$r_{\mu = \{a, b\}} = \mathrm{Re} \left\{ 1 - \frac{1}{\tilde{q}_\mu^2} \sqrt{\left(\tilde{q}_\mu^2 + i\tilde{\xi} \right)^2 - 4\tilde{q}_\mu^2} \right\}, \quad (44)$$

where the effective Fermi momentum $p_F = \sqrt{\pi x}$ remains the same and we define

$$\tilde{q}_a^2 = \sqrt{\frac{\beta_1}{\beta_2}} \tilde{q}_1^2 + \sqrt{\frac{\beta_2}{\beta_1}} \tilde{q}_2^2, \quad \tilde{q}_b^2 = \sqrt{\frac{\beta_1}{\beta_2}} \tilde{q}_2^2 + \sqrt{\frac{\beta_2}{\beta_1}} \tilde{q}_1^2. \quad (45)$$

The calculation of the Néel–spin-liquid phase boundary line λ_{c1} is analogous to the case of circular Fermi pockets presented in the Sec. IV A. Eq. (36) is replaced by

$$1 - \lambda_{c1} \propto \exp \left[-\frac{2\rho_s (\langle \vec{n}_\perp^2 \rangle_c - \phi)}{\beta x f(\beta_1, \beta_2)} \right], \quad (46)$$

where $f(\beta_1, \beta_2)$ is a smooth symmetric function that only weakly depends on the ratio β_1 / β_2, for circular pockets $f(\beta, \beta) = 1$. So here the ellipticity does not result in a significant effect.

Importantly, for $\lambda > 1$ the ellipticity results in a qualitative effect. It pins the wave vector of the spin spiral to the antinodal direction, $\mathbf{Q} = (Q, 0)$ or $\mathbf{Q} = (0, Q)$. To see this, one has again to write down the denominator of the magnon Green's function in the spin-liquid phase, similar to Eq. (40), but with an account of anisotropic polarization operator Eqs. (44). Then for the nodal direction, $\mathbf{Q} = Q/\sqrt{2}(1, \pm 1)$, the denominator has a minimum at

$$Q = 2p_F \left(\frac{\beta_2}{\beta_1} \right)^{1/4}, \quad (47)$$

and the instability condition Eq. (41) is replaced by

$$\Delta^2 - 4c^2 p_F^2 \sqrt{\frac{\beta_2}{\beta_1}} (\lambda - 1) = 0. \quad (48)$$

On the other hand, for the antinodal direction, $\mathbf{Q} = (Q, 0)$ or $\mathbf{Q} = (0, Q)$, the denominator has a minimum at the wave vector

$$Q = \frac{2p_F}{\sqrt{\frac{1}{2} \left(\sqrt{\frac{\beta_1}{\beta_2}} + \sqrt{\frac{\beta_2}{\beta_1}} \right)}}, \quad (49)$$

and the instability condition reads

$$\Delta^2 - 4c^2 p_F^2 (\lambda - 1) \frac{2}{\sqrt{\frac{\beta_1}{\beta_2}} + \sqrt{\frac{\beta_2}{\beta_1}}} = 0. \quad (50)$$

This condition is satisfied at a smaller value of λ than the diagonal spin-spiral condition Eq. (48). Hence the spin spiral always condensates in the antinodal direction. The wave vector is given by Eq. (49), but this equation is valid only at very small x.

In spite of the pinning of the spin-spiral direction the spin-liquid borderline is not changed much compared to Eq. (42). Taking into account the Fermi pocket ellipticity, the equation for the critical line reads

$$\lambda_{c2} - 1 \propto \exp \left(-\frac{2\rho_s (\langle \vec{n}_\perp^2 \rangle_c - \phi)}{\beta x f(\beta_1, \beta_2)} \right). \quad (51)$$

V. ULTRAVIOLET CUTOFF, LINDEMANN CRITERION, NUMERICAL CALCULATIONS, AND COMPARISON WITH EXPERIMENT

A. Ultraviolet cutoff

Let us first determine Λ_q. At zero doping, $x = 0$, Eq. (25) reads

$$\langle \vec{n}_\perp^2 \rangle = \frac{2}{\chi_\perp} \int_0^{\Lambda_q} \frac{d^2 q}{(2\pi)^2} \int_{-c_0 \Lambda_q}^{c_0 \Lambda_q} \frac{d\xi}{2\pi} \frac{1}{\xi^2 + c_0^2 q^2}. \quad (52)$$

This corresponds to the usual 2D Heisenberg model on the square lattice where we know well that the staggered magnetization is $\langle S_z \rangle \approx 0.30$. This corresponds to $\langle 2S_z \rangle = \langle n_z \rangle \approx 1 - \frac{1}{2}\langle \vec{n}_\perp^2 \rangle \approx 0.6$. Hence at $\langle \vec{n}_\perp^2 \rangle = 0.8$. The upper limit of integration in Eq. (52) must be tuned to reproduce this value. From here we find

$$\Lambda_q \approx 1.2 = 0.19(r.l.u) . \tag{53}$$

This is the value of Λ_q for crossover from the intermediate regime to the ultraviolet regime that was first introduced in Fig. 2 based on experimental data.

B. Lindemann criterion

The concept of the critical value of magnetic fluctuation is defined by Eq. (35). Here we quantify the value of $\langle \vec{n}_\perp^2 \rangle_c$, the Lindemann criterion. This value depends on dimensionality and probably on some details of fluctuations. In Ref. [16], comparing the field theory with density matrix renormalization group (DMRG) calculations, we found that for 1D integer spin Haldane chain $\langle \vec{n}_\perp^2 \rangle_c \approx 0.6$. Interestingly, the renormalization group in this case gives $\langle \vec{n}_\perp^2 \rangle_c = 1$, Ref. [35], although DMRG is more reliable. In the same paper [16], we argue that for 2D Ioffe-Larkin spin liquid

$$\langle \vec{n}_\perp^2 \rangle_c \approx 1 . \tag{54}$$

Here we would like also make a comparison of our approach with Takahashi's modified spin-wave theory [34] or Schwinger boson mean field technique [36]. For 2D Heisenberg model at nonzero temperature T, these methods work reasonably well. In this case, the equation similar to Eq. (25) reads

$$\langle \vec{n}_\perp^2 \rangle_c = \frac{2}{\chi_\perp} \int_0^{\Lambda_q} \frac{1}{\omega_q} \left(\frac{1}{e^{\omega_q/T} - 1} + \frac{1}{2} \right) \frac{d^2q}{(2\pi)^2} . \tag{55}$$

Here $\omega_q = \sqrt{c_0^2 q^2 + \Delta_T^2}$, Δ_T is the temperature related "gap." At $T \ll J$ we can rewrite Eq. (55) as

$$\langle \vec{n}_\perp^2 \rangle_c = \frac{4T}{\pi J} \ln \left(\frac{T}{\Delta_T} \right) + \frac{2\sqrt{2}}{\pi} \int_0^{\Lambda_q} dq . \tag{56}$$

The second term in this equation is the zero-temperature quantum fluctuation and, according to the discussion in the previous paragraph, this term is approximately equal to 0.8. On the other hand according to Ref. [34] the finite T gap is $\Delta_T \sim T e^{-2\pi \rho_s^{(r)}/T}$, where $\rho_s^{(r)} \approx 0.17J$ is the renormalized spin stiffness for the 2D Heisenberg model. Substitution of Δ_T in Eq. (56) gives $\langle \vec{n}_\perp^2 \rangle_c \approx 2$. This is the expected result since the Takahashi's modified spin-wave theory implicitly assumes the leading order expansion $\langle n_z \rangle = \langle \sqrt{1 - \vec{n}_\perp^2} \rangle \approx 1 - \frac{1}{2}\langle \vec{n}_\perp^2 \rangle$ and equating $\langle n_z \rangle$ to zero. This immediately gives the above condition. The value of $\langle \vec{n}_\perp^2 \rangle > 1$ looks strange keeping in mind the constraint $n^2 = 1$. The large fluctuation is a byproduct of linearization, which one necessarily does when working with strong fluctuations. It is known that for the 2D Heisenberg model at $T \neq 0$ the method works reasonably well for the correlation length [37]. However, when applied to a disordered system at zero temperature, the method gives the strange result that the physical gap is $2\Delta_T$, Ref. [36]. In this case, Δ_T is just an infrared cutoff unrelated to temperature.
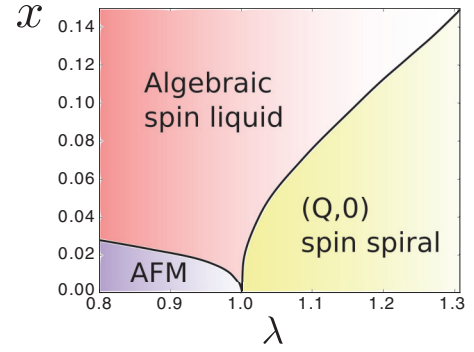

FIG. 6. Zero temperature $\lambda - x$ phase diagram of the modified $t - J$ model. The range of λ corresponding to cuprates is given by Eq. (9).

Moreover, application of the criterion $\langle \vec{n}_\perp^2 \rangle_c = 2$ to the Ioffe-Larkin spin liquid in 2D $J_1 - J_3$ model and to 1D Haldane spin chain gives results completely inconsistent with numerics [16]. Therefore, in the present work we use the criterion Eq. (54).

C. Numerical calculations and comparison with experimental data

As soon as the ultraviolet cutoff Eq. (53) and the quantum melting criterion Eq. (54) are fixed, we can find the phase diagram by solving numerically Eqs. (38) and (50). The phase diagram resulting from this calculation is presented in Fig. 6.

It is even more instructive to calculate the "gap" Δ defined by Eq. (37). The gap is determined from a numerical solution of Eq. (38). At $\omega = \Delta$, the magnetic response is maximum at $q = 0$, which for neutron scattering corresponds to $\mathbf{q} = (\pi, \pi)$. Therefore, Δ is identical to E_{cross} usually determined in neutron scattering [1]. The value of Δ depends on λ at a given doping x, for instance it vanishes at the transition line from the spin liquid to the AFM phase. However, at $\lambda > 1$ the dependence $\Delta(\lambda)$ is rather weak, this even includes the transition line from the spin liquid to the spin-spiral state. In this region, it is sufficient to calculate $\Delta(\lambda = 1) \approx E_{\mathrm{cross}}$. The result of this calculation is shown in Fig. 7 by the black solid line. There is an uncertainty in our calculations that is worth mentioning. In our calculation, we assume that the coupling constant g defined in Eq. (4) is momentum independent. Within the $t - J$ model, the coupling constant is $g = t\sqrt{Z_k Z_{k+q}}$. At small q we obtain $g = tZ$, where $Z = Z_{(\pi/2,\pi/2)}$. At doping $x \sim 0.1$ the Fermi momentum $p_F = \sqrt{\pi x} \sim 0.6$ and the typical value of momentum responsible for fluctuations, $q \sim 2p_F$, is quite large. At these values of momentum, the dependence of the quasiparticle residue on momentum becomes significant. Fitting numerical data obtained in SCBA we found that

$$Z_k \approx Z z_k , \quad z_k = 1 - 0.3 \frac{\epsilon_k}{J} , \tag{57}$$

where ϵ_k is given by Eqs. (2). Within the range of parameters corresponding to cuprates, the coefficient in the fit varies between 0.25 and 0.35. We take 0.3 as some effective value. The fit Eqs. (57) is valid when $Z_k \geqslant 0$, otherwise $Z_k = 0$. To account for the residue momentum dependence the expression
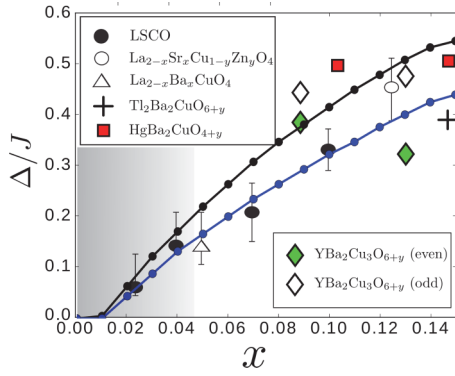
FIG. 7. E_{cross} versus doping. The black solid line shows the calculation without account of the momentum dependence of the holon residue. The blue solid line shows the calculation with an account of the holon residue momentum dependence. The range between these lines indicates the theoretical uncertainty of our calculation. Experimental data are shown by symbols [1,38–41]. Theoretical curves correspond to $\lambda = 1$, however, dependence of E_{cross} on λ is weak. Symbols at $x < 5\%$ correspond to LSCO (grey region), where physics is driven by localization. Comparison of theoretical calculations and experimental data at doping $x < 5\%$ is less justified.

under the sum $\sum_{k,\alpha}$ in the polarization operator Eq. (26) should be multiplied by $z_k z_{k+q}$ and all other formulas are unchanged. The gap Δ calculated with account of z_k is plotted in Fig. 7 by the blue solid line. The range between the black and the blue line indicates the theoretical uncertainty of our calculation. Symbols in Fig. 7 display experimental data. The agreement between the theory and the experiment is exciting. Our approach grasps the essential physics of the problem.

VI. SPIN-SPIN CORRELATION FUNCTION IN THE ALGEBRAIC SPIN-LIQUID PHASE

Here we consider the equal time spin-spin correlator,

$$C(r) = \langle \vec{n}(r) \cdot \vec{n}(0) \rangle. \quad (58)$$

There are two main messages of this section. (i) The correlator decays at the typical scale $r \sim 1/p_F \sim 1/\sqrt{x}$. This is true even in the limit when the gap is exponentially small, Eq. (39). (ii) There is a long-distance tail of the correlator which decays as $1/r^3$, so the spin liquid is algebraic.

Following Ref. [16], we represent the correlator as

$$C(\mathbf{r}) \approx 1 + \mathcal{P} - R + ..., \quad (59)$$

where

$$\mathcal{P}(r) = \langle \mathbf{n}_\perp(r) \cdot \mathbf{n}_\perp(0) \rangle, \quad R = \mathcal{P}(0) = \langle \mathbf{n}_\perp^2 \rangle. \quad (60)$$

The two-point correlator is normalized such that $C(0) = 1$. In the spin-liquid phase, the correlation function should vanish at large distances, $C(r \to \infty) \to 0$ and $\mathcal{P}(r \to \infty) \to 0$. This condition is consistent with Eq. (59) if we truncate the asymptotic expansion in Eq. (59), keeping only the terms explicitly presented there. The explicit expression for $\mathcal{P}$ immediately follows from Eq. (37):

$$\mathcal{P}(r) = \frac{1}{\pi \chi_\perp} \int_0^{\Lambda_q} dq\, q \int_0^{c\Lambda_q} \frac{d\xi}{2\pi} \frac{J_0(qr)}{\xi^2 + \Delta^2 + P^F(i\xi, q)}. \quad (61)$$
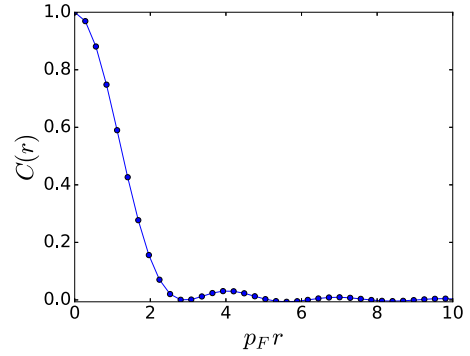

FIG. 8. Spin-spin equal time correlation function $C(r, t = 0) = \langle \mathbf{n}(r) \cdot \mathbf{n}(0) \rangle$ at the Lifshitz point, $\lambda = 1$. Here we take circular Fermi pockets, $\beta/J = 2$, doping $x = 0.1$.

Here J_0 is the Bessel function. Note that in this section, for simplicity we consider circular Fermi pockets. At $r = 0$ formula Eq. (61) is identical to Eq. (38).

The algebraic behavior of the correlator originates from the nonanalytic dependence on ξ in the polarization operator Eq. (32). Here we calculate the correlator at the Lifshitz point, $\lambda = 1$. Evaluation of the ξ integral in Eq. (61) in the limit $\Delta \to 0$ with logarithmic accuracy gives

$$\mathcal{P}(r) = \frac{\beta}{2\pi^2 \rho_s} \int_0^{2p_F} dq \sqrt{4p_F^2 - q^2}$$
$$\times \ln\left(1 + \frac{c^2}{\Delta^2} q \sqrt{4p_F^2 - q^2}\right) J_0(qr). \quad (62)$$

From here we come to the conclusions formulated in the beginning of the section. (i) The correlator $\mathcal{P}$ and hence the correlator C decays at the typical scale about $r \sim 1/p_F \sim 1/\sqrt{x}$. (ii) There is a long-distance tail of the correlator which decays as $1/r^3$, so the spin liquid is algebraic.

We evaluate the long-distance asymptotics, $r \to \infty$, in Eq. (62) using the stationary phase approximation. The leading contribution to the integral comes from the endpoints of the integration, $q = 0$ and $q = 2p_F$. Performing Tailor expansion of the logarithm in Eq. (62), in the vicinity of the endpoints we obtain that the asymptotics contain a power tail $1/r^3$ as well as the oscillating power tail $\propto \frac{\cos 2p_F r}{r^{5/2}}$, a sort of Friedel oscillations. The $1/r^3$ asymptotics is due to the left endpoint $q = 0$ and the oscillating part of the asymptotics is due to the right endpoint $q = 2p_F$ of the integration. However, the oscillating power tail is present only in the case of the circular Fermi pockets. In fact, the oscillations are strongly suppressed for elliptic pockets (some algebraically decaying oscillations survive for the nodal direction), while the points (i) and (ii) are generic. Equation (62) is valid only at a very small doping x where the logarithmic approximation makes sense. On the other hand, numerical integration in Eq. (61) is straightforwrd. The correlator $C(r)$ calculated by performing numerical integration at $x = 0.1$ in Eq. (61) is plotted in Fig. 8.

VII. CONCLUSION

In the present paper, we demonstrate that there is a hidden dimensionless parameter λ, which drives quantum magnetic criticality in the extended $t - J$ model at low doping x. Using an effective field theory, we study the zero temperature $\lambda - x$ phase diagram of the model. The phase diagram is shown schematically in Fig. 1(b) and quantitatively in Fig. 6. The most important feature of the phase diagram is the quantum tricritical Lifshitz point at $x = 0$, $\lambda = 1$. We calculate parameters of the effective theory using SCBA. Using this approximation, we show that underdoped cuprates are close to the quantum tricritical point. The three phases "meet" at the tricritical point: Néel antiferromagnet, spin spiral with antinodal direction of the spiral wave vector, and algebraic spin liquid.

We believe that underdoped cuprates belong either to the spin-liquid phase or they are on the borderline between the spin liquid and the antinodal spin spiral. We study properties of the spin-liquid phase and demonstrate algebraic decay of equal time spin-spin correlation. We calculate the energy position E_{cross} of the inelastic neutron scattering response maximum at $\boldsymbol{q} = (\pi, \pi)$ and compare our results with experiments. Theoretical curves and experimental data are displayed in Fig. 7. We also explain softening of magnons in the intermediate regime observed in inelastic neutron scattering, see Fig. 5.

[1] M. Fujita, H. Hiraka, M. Matsuda, M. Matsuura, J. M. Tranquada, S. Wakimoto, G. Xu, and K. Yamada, J. Phys. Soc. Jpn. **81**, 011007 (2012).

[2] C. Stock, W. J. L. Buyers, Z. Yamani, Z. Tun, R. J. Birgeneau, R. Liang, D. Bonn, and W. N. Hardy, Phys. Rev. B **77**, 104513 (2008).

[3] V. Hinkov, D. Haug, B. Fauque, P. Bourges, Y. Sidis, A. Ivanov, C. Bernhard, C. T. Lin, and B. Keimer, Science **319**, 597 (2008).

[4] D. Haug, V. Hinkov, Y. Sidis, P. Bourges, N. B. Christensen, A. Ivanov, T. Keller, C. T. Lin, and B. Keimer, New J. Phys. **12**, 105006 (2010).

[5] P. W. Anderson, Science **235**, 1196 (1987).

[6] V. J. Emery, Phys. Rev. Lett. **58**, 2794 (1987).

[7] F. C. Zhang and T. M. Rice, Phys. Rev. B **37**, 3759 (1988).

[8] B. I. Shraiman and E. D. Siggia, Phys. Rev. B **42**, 2485 (1990).

[9] A. V. Chubukov and K. A. Musaelian, Phys. Rev. B **51**, 12605 (1995).

[10] O. P. Sushkov and V. N. Kotov, Phys. Rev. B **70**, 024503 (2004).

[11] A. I. Milstein and O. P. Sushkov, Phys. Rev. B **78**, 014501 (2008).

[12] L. B. Ioffe and A. I. Larkin, J. Mod. Phys. B **2**, 203 (1988).

[13] O. P. Sushkov and V. N. Kotov, Phys. Rev. Lett. **94**, 097005 (2005).

[14] A. Luscher, A. I. Milstein, and O. P. Sushkov, Phys. Rev. Lett. **98**, 037001 (2007).

[15] O. P. Sushkov, Phys. Rev. B **79**, 174519 (2009).

[16] Y. A. Kharkov, J. Oitmaa, and O. P. Sushkov, arXiv:1804.04308 [Phys. Rev. B (to be published)].

[17] M. Le Tacon, G. Ghiringhelli, J. Chaloupka, M. Moretti Sala, V. Hinkov, M. W. Haverkort, M. Minola, M. Bakr, K. J. Zhou, S. Blanco-Canosa *et al.*, Nat. Phys. **7**, 725 (2011).

[18] T. Imai, C. P. Slichter, K. Yoshimura, and K. Kosuge, Phys. Rev. Lett. **70**, 1002 (1993).

[19] S. Sachdev, Phys. Rev. B **49**, 6770 (1994).

[20] O. P. Sushkov, Phys. Rev. B **54**, 9988 (1996).

[21] F. Onufrieva, Phys. Rev. B **95**, 125110 (2017).

[22] S. Chatterjee, S. Sachdev, and M. S. Scheurer, Phys. Rev. Lett. **119**, 227002 (2017).

[23] M. S. Scheurer, S. Chatterjee, W. Wu, M. Ferrero, A. Georges, and S. Sachdev, Proc. Nat. Acad. Sci. U.S.A. **115**, E3665 (2018).

[24] O. K. Andersen, A. I. Liechtenstein, O. Jepsen, and F. Paulsen, J. Phys. Chem. Solids **56**, 1573 (1995); E. Pavarini, I. Dasgupta, T. Saha-Dasgupta, O. Jepsen, and O. K. Andersen, Phys. Rev. Lett. **87**, 047003 (2001).

[25] O. P. Sushkov, G. A. Sawatzky, R. Eder, and H. Eskes, Phys. Rev. B **56**, 11769 (1997).

[26] O. P. Sushkov, Phys. Rev. B **84**, 094532 (2011).

[27] V. N. Kotov and O. P. Sushkov, Phys. Rev. B **70**, 195105 (2004).

[28] P. Bourges, H. F. Fong, L. P. Regnault, J. Bossy, C. Vettier, D. L. Milius, I. A. Aksay, and B. Keimer, Phys. Rev. B **56**, R11439 (1997).

[29] O. J. Lipscombe, B. Vignolle, T. G. Perring, C. D. Frost, and S. M. Hayden, Phys. Rev. Lett. **102**, 167002 (2009).

[30] B. Vignolle, S. M. Hayden, D. F. McMorrow, H. M. Ronnow, B. Lake, C. D. Frost, and T. G. Perring, Nat. Phys. **3**, 163 (2007).

[31] W. Chen and O. P. Sushkov, Phys. Rev. B **88**, 184501 (2013).

[32] W. Chen, O. P. Sushkov, and T. Tohyama, Phys. Rev. B **84**, 195125 (2011).

[33] R. Coldea, S. M. Hayden, G. Aeppli, T. G. Perring, C. D. Frost, T. E. Mason, S.-W. Cheong, and Z. Fisk, Phys. Rev. Lett. **86**, 5377 (2001).

[34] M. Takahashi, Phys. Rev. Lett. **58**, 168 (1987).

[35] I. Affleck, J. Phys.: Condens. Matter **1**, 3047 (1989).

[36] A. Auerbach and D. P. Arovas, Phys. Rev. Lett. **61**, 617 (1988).

[37] E. Manousakis, Rev. Mod. Phys. **63**, 1 (1991).

[38] M. K. Chan, C. J. Dorow, L. Mangin-Thro, Y. Tang, Y. Ge, M. J. Veit, G. Yu, X. Zhao, A. D. Christianson, J. T. Park, *et al.*, Nat. Commun. **7**, 10819 (2016).

[39] M. K. Chan, Y. Tang, C. J. Dorow, J. Jeong, L. Mangin- Thro, M. J. Veit, Y. Ge, D. L. Abernathy, Y. Sidis, Ph. Bourges *et al.*, Phys. Rev. Lett. **117**, 277002 (2016).

[40] S. Pailhès, C. Ulrich, B. Fauque, V. Hinkov, Y. Sidis, A. Ivanov, C. T. Lin, B. Keimer, and P. Bourges, Phys. Rev. Lett. **96**, 257001 (2006).

[41] H. He, P. Bourges, Y. Sidis, C. Ulrich, L. P. Regnault, S. Pailhes, N. S. Berzigiarova, N. N. Kolesnikov, and B. Keimer, Science **295**, 1045 (2002).